International Journal of Solids and Structures 69–70 (2015) 106–120

Contents lists available at ScienceDirect

International Journal of Solids and Structures

journal homepage: www.elsevier.com/locate/ijsolstr

An anisotropic large displacement cohesive zone model for fibrillar and crazing interfaces

M. Paggi [a,*], J. Reinoso [a,b]

[a] IMT Institute for Advanced Studies Lucca, Piazza San Francesco 19, 55100 Lucca, Italy
[b] Group of Elasticity and Strength of Materials, School of Engineering, University of Seville, Camino de los Descubrimientos s/n, 41092 Seville, Spain

ARTICLE INFO

Article history:
Received 8 October 2014
Received in revised form 24 January 2015
Available online 10 June 2015

Keywords:
Anisotropic cohesive zone model
Fibrillar interfaces
Large displacements
Photovoltaics
Bonding of paper tissue
Crazing of polymers

ABSTRACT

A new cohesive zone model to describe fracture of interfaces with a microstructurs made of fibrils with statistically distributed in-plane and out-of-plane orientations is proposed. The elementary force–displacement relation of each fibril is considered to obey the peeling theory of a tape, although other refined constitutive relations could be invoked for the adhesive constitutive response without any lack of generality. The proposed consistent 2D and 3D interface finite element formulations for large displacements account for both the mechanical and the geometrical tangent stiffness matrices, required for implicit solution schemes. After a preliminary discussion on model parameters identification, it is shown that by tailoring the spatial density of fibrils at different orientations can be a way to realize innovative interfaces enhancing adhesion or decohesion, depending on the need. For instance, it can be possible to realize microstructured adhesives to facilitate debonding of the glass cover in photovoltaic modules to simplify recycling purposes. Moreover, the use of probability distribution functions describing the density of fibrils at different orientations is a very effective approach for modeling the anisotropy in the mechanical bonding between paper tissues and for simulating the complex process of crazing in amorphous polymers.

© 2015 Elsevier Ltd. All rights reserved.

1. Introduction

Interfaces with microstructures have been observed in the transition zones between several natural and artificial systems and have been subject of intense research. A pioneering theory of structured interfaces reinforced by fibers modeled as linear elastic bars has been proposed in Bigoni and Movchan (2002) and Bertoldi et al. (2007a,b,c) to deal with interfaces with microstructures like those of the metacarpal bone of a vulture-wing, the pinctada nacre, the short glass–fiber-reinforced polypropylene, the crack tip in polystyrene, the meninges surrounding the human brain, the cross-section of a palm petiole, and the pyrolyzed wood infiltrated with Silicon. The derived results have emphasized the role of the interface microstructure on the properties of a linear elastic system, both in statics and in dynamics.

Along this line of research, attempts to describe the nonlinear behavior of finite thickness interfaces by developing synthetic traction-inelastic separation relations, or cohesive zone models, have been proposed in Paggi and Wriggers, 2011a,b, 2012 for polycrystalline materials, explicitly considering the evolution of damage in these finite thickness regions. A different set of computational approaches, that aim at providing a further insight into the fibrillation using micromechanics-based models and including viscoelastic effects, has been developed in Allen and Searcy (2001) and Estevez et al. (2000), among others. As an alternative route, multi-scale computational methods have been proposed in Matous et al. (2008) to derive the cohesive zone model response of particle reinforced adhesives by a multi-scale analysis explicitly taking into account the finite element representation of the interface microstructure. Geers and coworkers (van den Bosch et al., 2008b; Vossen et al., 2014) have also recently developed a multi-scale strategy to simulate the mechanism of fibrilation in the delamination of polymer-coated metal sheets. These investigations are based on a series of experimental works devoted to the understanding of the fibrillation processes in polymers (see Kramer and Berger (1990), Creton and Lakrout (2000), Hoefnagels et al. (2010), Desai et al. (2011) and the references therein given) which basically regard: (1) the voids formation along the interface, (2) the generation of load bearing crazes (fibrils), and (3) the final failure of such fibrils, leading to interface crack propagation.

In parallel with these studies, mostly dealing with fracture of imperfect finite thickness interfaces joining dissimilar materials,

* Corresponding author. Tel.: +39 0583 4326 604; fax: +39 0583 4326 565.
E-mail addresses: marco.paggi@imtlucca.it (M. Paggi), jreinoso@us.es (J. Reinoso).

http://dx.doi.org/10.1016/j.ijsolstr.2015.04.042
0020-7683/© 2015 Elsevier Ltd. All rights reserved.

another impressive line of research has focused during the last decade on the morphology of surfaces of living systems and its connection with their adhesion capabilities. The analysis of pads and surfaces of insects, spiders and lizards have revealed the presence of a complex texturing able to maximize adhesion and tolerate interfacial crack-like flaws caused by surface roughness (Gao et al., 2004; Yao and Gao, 2008). A notable example are the pads of Tokay gecko, showing a hierarchical assembly of microscale hairs, called *setae*, branching off into nanoscale *spatulae* (Huber et al., 2005; Scherge and Gorb, 2001; Pugno and Lepore, 2008; Pugno et al., 2011; Lepore et al., 2012). Extensive modeling of the gecko attachment/detachment system has provided a valuable insight into the mechanisms promoting the adhesion of natural and bio-inspired interfaces (Gao et al., 2005; Yao and Gao, 2007; Yao et al., 2008). At the microscale, the adhesive behavior of spatulae has been successfully modeled as an elastic tape (Gao et al., 2005), conforming with the semi-analytical adhesion theory by Kendall (1975). The ability to tolerate roughness was finally explained by a hierarchical assembly of fractal type of spatulae and hairs (Yao and Gao, 2006, 2008). Moreover, for releasable adhesion, the macroscopic elastic anisotropy was found to vary the adhesion strength significantly with the direction of pulling, leading to an orientation-controlled switch between attachment and detachment scenarios (Yao and Gao, 2006; Chen and Gao, 2007; Chen et al., 2008).

The bottom-up design principles of structured interfaces and surfaces emerging from the aforementioned state-of-the-art on the subject open a frontier of research in the design of novel adhesives for a wide range of engineering applications. In the present work, an anisotropic interface constitutive law based on the adhesion mechanisms of fibrils at the microscale is proposed. The key idea is to derive a traction-separation law or cohesive zone model (CZM) based on bottom-up considerations. The interface region is modeled at the micro-scale as a surface covered by fibrils adhering to a substrate with certain in-plane and out-of-plane orientations. The force–elongation relation of each fibril will provide an elementary contribution to the overall cohesive traction-separation relation of the interface resulting from their spatial integration. As a result of the orientation-dependent tractions stemming from the classical equations of the peeling theory proposed by Kendall (1975), this basic model will provide an adhesion force dependent on the mode of deformation experienced by the interface. This formulation is further enhanced by showing that a possible way to maximize or minimize adhesion along specific directions can be achieved by introducing a probability distribution function to describe the density of fibrils with a given inclination, instead of assuming a uniform distribution. From the numerical standpoint, within the context of nonlinear FEM, the 2D and 3D versions of the adhesion/decohesion model herein proposed is incorporated into the large deformation interface element recently developed in Reinoso and Paggi (2014), providing a robust and versatile computational framework for engineering simulations.

The paper is organized as follows. Section 2 is concerned with the formulation of an anisotropic cohesive zone model that accounts for interfaces with a microstructural arrangement based on fibril distributions for 2D and 3D applications. Since the developed model is expected to have a special impact on maximizing adhesion or detachment of thin-walled structures undergoing large-displacements, details concerning the 3D generalization of the novel interface element formulation proposed in Reinoso and Paggi (2014) are given in Section 3. This interface element provides a consistent derivation to deal simultaneously with material and geometrical nonlinearities in those detachment applications where both nonlinearities have a relevant role. Using this computational method, applications related to the understanding of the behavior of cellulose fibrils in paper tissue bonding, and a new possibility to facilitate disassembling operations in photovoltaic modules for recycling purposes are investigated in Section 4. Finally, the main conclusions of the present contribution along with its further potential capabilities are addressed in Section 5.

2. Derivation of the anisotropic cohesive zone model: adhesion control based on the peeling theory

In this section the anisotropic interface constitutive relation based on the peeling theory for controlling the adhesion of interfaces with a fibrillar microstructure is derived. After introducing a two-dimensional formulation, its generalization to three-dimensional problems is presented. The corresponding mathematical treatments are kept separate in this section since they have different degrees of complexity as far as the finite element implementation detailed in Section 3 and in Appendix is concerned.

2.1. Two-dimensional constitutive model

Let assume the microstructural arrangement of the interface be covered by a collection of elastic fibrils or spatulae perfectly joined to the body sharing the upper side of the interface and bonded to the opposite side as an adhesive tape, see Fig. 1. Introducing as customary a local reference system defined by the tangent and normal vectors to the middle-line of the interface, which is updated during the deformation process, these fibrils may have different instant inclination angles β, possibly covering all the values ranging from zero to π.

Regarding the initial value of the angle β, different options may be considered. When a surface is adhering on a substrate by the action of fibrils, as in Fig. 1, their inclination angle can obey a statistical distribution. For instance, groups of polymer chains bridging a crazing crack may have a uniform distribution of orientations, see e.g. Fig. 2.

In case of hairy pads of living insects or Gecko's spatulae, the angle β is in general different from zero and it is influenced by the statistics of surface texturing and roughness which govern the contact angles with the spatulae. As recently investigated in Zhou et al. (2014), the angle β can have a deterministic value only if the texturing is regular as in the form of cylinders, see Fig. 3(a), or in case of sinusoidal waviness as considered in Gillies and Fearing (2014). In the more general case of random roughness, a statistical distribution of angles β is expected to arise from the actual distribution of the local slopes of the profile height field. As an example, the probability distribution density function of angles β computed from the statistical analysis of the profiles of a fractal surface with $D = 2.3$ and generated with the random midpoint displacement algorithm is shown in Fig. 3(a), and it resembles a Gaussian distribution.

We also admit the possibility to have a nonuniform distribution obtained from the subtraction of a Gaussian distribution from a uniform distribution. This can be used to model an interface with a reduced density of fibrils centered around a given orientation. The resulting probability distribution function will present a reduced frequency of fibrils along the pre-selected orientation, thus weakening adhesion along that specific direction. This configuration will be referred to as *nonuniform distribution for detachment* in the sequel.

In summary, with the aim of accounting for the initial microstructural arrangement of interfaces based on fibril distributions, we propose the introduction of a factor $a_f(\beta)$ that will provide the frequency of fibrils with an initial out-of-plane inclination β:

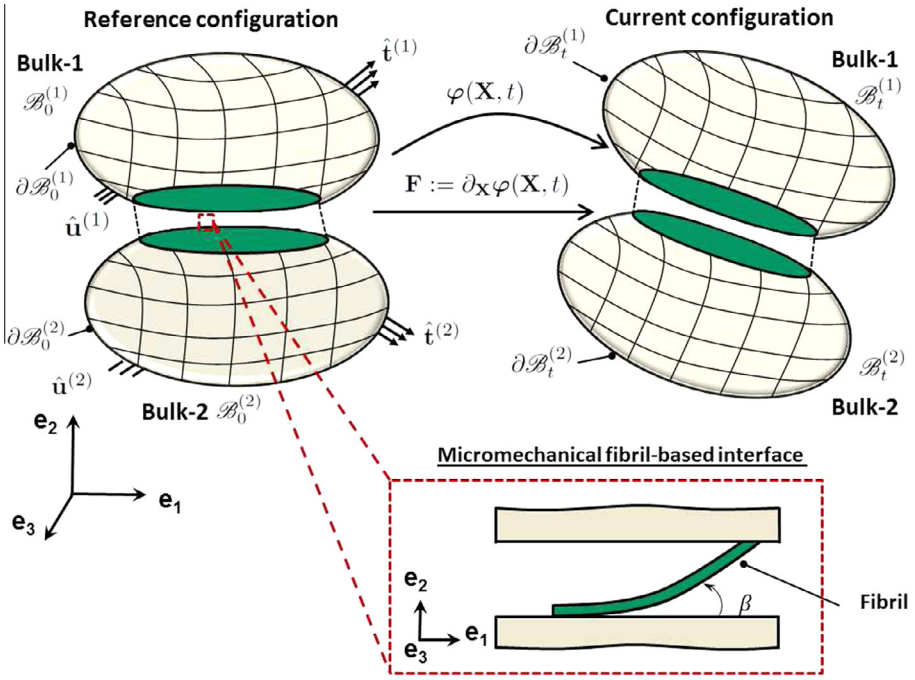

Fig. 1. Sketch of a fibril or a spatula inclined by an instant angle β with respect to the line tangent to the interface.

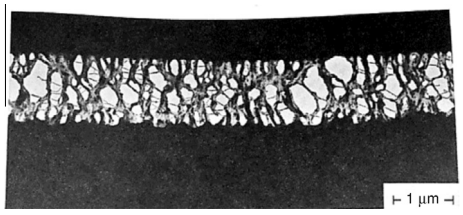

Fig. 2. Crazing of a polymer showing fibers bridging a crack with a uniform distribution of inclinations, adapted from http://www.kamakurapen.com/Archive/Crazing.html.

$$a_f(\beta)=\begin{cases}1, & \text{uniform distribution}\\ \frac{1}{\sigma\sqrt{2\pi}}\exp\frac{-(\beta-\mu)^2}{2\sigma^2}, & \text{nonuniform distr.}\\ \frac{k_1}{\sigma\sqrt{2\pi}}-\frac{1}{\sigma\sqrt{2\pi}}\exp\frac{-(\beta-\mu)^2}{2\sigma^2}, & \text{nonuniform distr. for detachment}\end{cases} \quad (1)$$

where μ_β is the mean value of the angle β where the distribution function is centered and σ_β is the root mean square value of the Gaussian distribution. The coefficient k_1 is a free parameter such that $a_f(\beta)$ is maintained strictly positive valued. Without any loss of generality, other distribution functions or even discrete empirical frequency histograms could be adopted in the numerical scheme. The coefficient $a_f(\beta)$ acts as a penalizing factor in case of nonuniform distributions of spatial densities of fibrils with respect to their inclination, since this parameter is less then or at most equal to unity, see an example in Fig. 4.

During the deformation process, the interface undergoes a relative displacement $\mathbf{g}_{\text{loc}}$, whose tangential and normal components are denoted by $g_{\text{loc,t}}$ and $g_{\text{loc,n}}$, respectively. In principle, all the fibers with their respective inclination may contribute to the load transfer. Therefore, the total bridging load would be the result

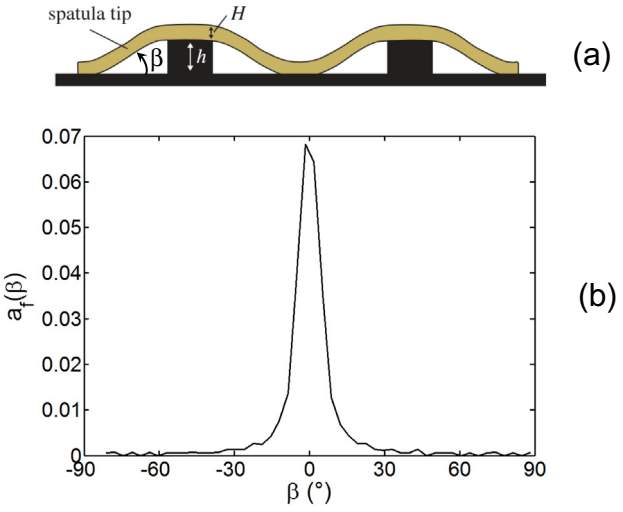

Fig. 3. (a) A sketch of a hair of a living insect inclined due to the presence of a deterministic surface texture (adapted from Zhou et al., 2014). (b) A distribution of inclination angles β arising from the statistical distribution of profile slopes of a numerically generated fractal rough surface with fractal dimension $D=2.3$.

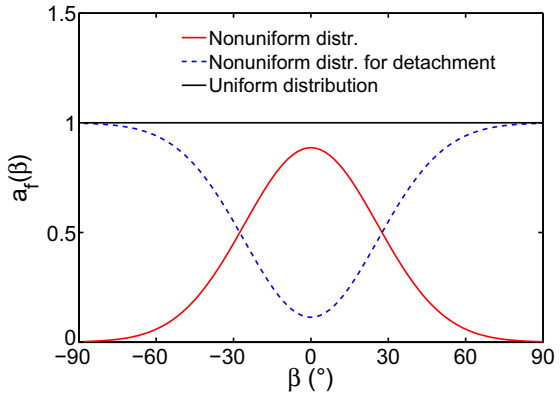

Fig. 4. The coefficient $a_f(\beta)$ representing the distribution of fibril orientations ($\mu=0^\circ, \sigma=0.45$ rad).

of the integral of the fibril force contributions for the corresponding penalizing factor that takes into account the angle deviation of the fibril with respect to β. However, in some cases, it is possible to simplify such a complex bridging mechanism by noting that there is often a predominant fibril orientation contributing to the peeling force. Specifically, this dominating fibril angle is the Mixed Mode deformation angle $\psi = \arctan\left(g_{\mathrm{loc,n}}/g_{\mathrm{loc,t}}\right)$. This assumption results into a simpler and a bit conservative formulation since the contributions of the fibrils with other orientations are not accounted for and only the fibrils with $\beta = \psi$ are considered as active. An experimental evidence confirming this assumption has been obtained for cellulose fibers bridging cracks in a thin paper tissue subjected to a tensile test, see a SEM image in Fig. 5(a). This mechanical testing has been performed in the Laboratory of the Research Unit MUSAM – Multi-scale Analysis of Materials at IMT Lucca, using the testing stage DEBEN 5000S located inside a SEM Zeiss EVO MA15. Clearly, the fibrils inclined with an angle ψ (fibrils aligned along the red arrow denoting the direction of loading) are in tension while the others tend to be unloaded. It is therefore reasonable to expect the fibrils in tension provide the major contribution to the load transfer.

Another instance supporting the assumption of an orientation $\beta = \psi$ of the active fibrils, but based on a totally different mechanism, is crazing in polymeric films. In this case, void formation leads to crazes all oriented with the same inclination enforced by the Mixed Mode deformation angle, see Fig. 5(b) taken from Desai et al. (2011). A subsequent modification of the interface inclination leads to a re-orientation of all the crazes. Therefore, this kind of phenomenon can be captured by the assumption of $\beta = \psi$ and using $a_f(\beta) = 1$, since all the fibrils are active and the *whole* population of fibrils re-orientates itself to follow the deformation process.

Based on these modeling assumptions confirmed by the experimental observation, the set of fibrils activated by the loading process are those with an angle β given by:

$$\beta(g_{\mathrm{loc,t}}, g_{\mathrm{loc,n}}) = \begin{cases} \arctan\left(\frac{g_{\mathrm{loc,n}}}{g_{\mathrm{loc,t}}}\right), & \text{if } \beta \geqslant 0,\ g_{\mathrm{loc,t}} \neq 0 \\ \pi/2, & \text{if } \beta \geqslant 0,\ g_{\mathrm{loc,t}} = 0 \\ \arctan\left(\frac{g_{\mathrm{loc,n}}}{g_{\mathrm{loc,t}}}\right) + \pi, & \text{if } g_{\mathrm{loc,t}} < 0 \end{cases} \tag{2}$$

The angle β is updated during the simulation by computing the displacement gaps between the adjacent flanks of the interface, in this way including geometrically nonlinear effects into the interface model. For a given angle β, the penalizing factor $a_f(\beta)$ in Eq. (1) is computed, depending on the material under consideration and the physical phenomenon to model.

According to the adhesion theory of an elastic tape (Kendall, 1975), the maximum peeling traction $\mathbf{t}$ at debonding (force per unit out-of-plane thickness) of an elastic fibril of Young modulus E_f, width w_f, and interfacial adhesion energy G, depends on the peeling angle β as:

$$\|\mathbf{t}(\beta)\| = E_f w_f \left[\sqrt{(1-\cos\beta)^2 + \frac{2G}{E_f t}} - (1-\cos\beta)\right] \tag{3}$$

where $\|\bullet\|$ stands for the Euclidean norm of the quantity $\bullet$. According to this theory, $\mathbf{t}$ has its maximum in correspondence to $\beta = 0^\circ$ and then it rapidly decays by increasing β, see Fig. 6 and similar plots in Kendall (1975) and Gao et al. (2005). It is worth mentioning that, as investigated in Begley et al. (2013), the Kendall solution can be interpreted as a limit case of a more general theoretical framework including frictional effects, which are not accounted in the present study. Nevertheless, the robustness of the proposed formulation relies on the fact that any kind of peeling model can be easily incorporated into the subsequent numerical scheme without any loss of generality.

The value of the maximum peeling traction corresponding to a given deformation angle ψ, which is assumed to equal β at each instantaneous deformation level, is finally given by $\mathbf{T} = a_f \mathbf{t}$, where

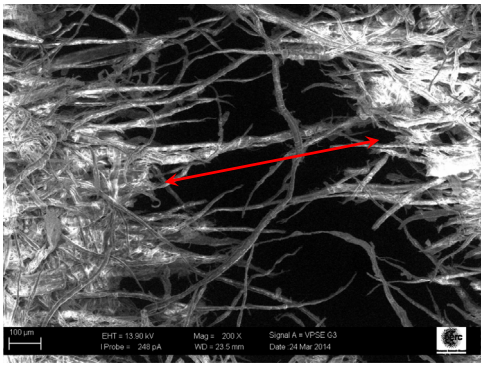

(a) Fibrils in paper tissue

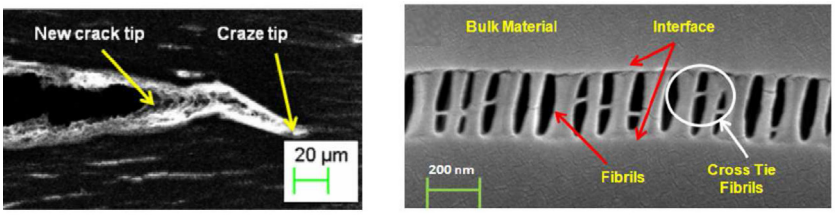

(b) Fibrils in polymer crazing at different magnifications

Fig. 5. (a) Cellulose fibrils bridging a crack. Note the prevailing alignment of the fibrils in the direction of loading and therefore with the deformation angle, see the red arrow in the online version of the article. The SEM image is taken under variable pressure conditions (VPSE sensor) at 13.9 kV, 200× magnification and a working distance of 23.5 mm. (b) Re-orientation of fibrils observed during polymer crazing, adapted from Desai et al. (2011). (For interpretation of the references to color in this figure legend, the reader is referred to the web version of this article.)

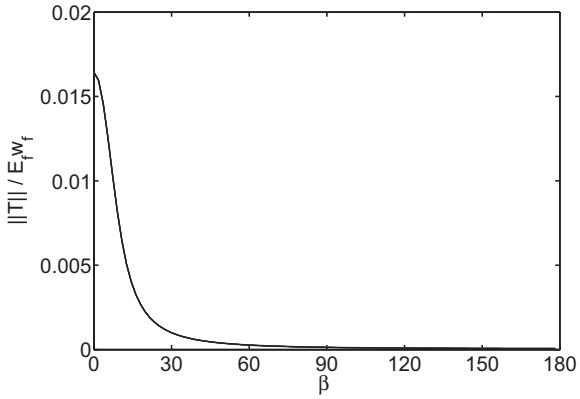

Fig. 6. Dimensionless modulus of the maximum peeling force **T** vs. peeling angle β.

the multiplying coefficient a_f takes into account the distribution of fibrils with a certain angle β along the interface.

Moreover, in the determination of the traction-displacement relation, that is integrated over the interface segment to compute the adhesive forces for each interface separation, each fibril is supposed to respond linearly to an applied force until the critical magnitude of the peeling force $\|\mathbf{t}(\beta)\|$ is reached. After that, we assume the part of the fibril in adhesion with the substrate is short enough so that it is no longer able to withstand any further load and a tension cut-off takes place. This tension cut-off idealization of the traction-separation law is supported by experimental evidence during crazing of polymers, see Desai et al. (2011) and further comments given in Section 4.

Introducing the modulus λ of the relative opening displacement vector $\mathbf{g}_{\rm loc}$, $\lambda = \sqrt{g_{\rm loc,t}^2 + g_{\rm loc,n}^2}$, the complete interface tractions-separation constitutive relation becomes:

$$T_n(\beta) = \|\mathbf{T}\| \frac{\lambda}{\|\mathbf{g}_{\rm loc,cr}\|} \sin\beta \tag{4a}$$

$$T_t(\beta) = \|\mathbf{T}\| \frac{\lambda}{\|\mathbf{g}_{\rm loc,cr}\|} \cos\beta \tag{4b}$$

where T_t and T_n are, respectively, the tangential and the normal components of the total traction vector **T**.

As clearly emerges from Fig. 6, the traction $\|\mathbf{T}(\beta)\|$ is maximum for $\beta = 0$ and then it decreases by increasing the angle β. Therefore, a system of fibrils displays its maximum adhesion in case of pure Mode II, i.e., for $\beta = 0$. On the other hand, the maximum peeling force for a pure Mode I problem ($\beta = \pi/2$) is much smaller. In case of a nonuniform distribution of fibrils modeled via the adhesion factor a_f, this trend can be suitably modified by tailoring the interface response to the specific needs. In Fig. 7(a), for instance, the adhesion along a given angle μ_β can be enhanced by assuming a Gaussian distribution of fibrils centered in μ_β and with a r.m.s. $\sigma_\beta = 0.14$ rad. Another possibility is to enhance detachment along a given angle μ_β as in Fig. 7(b), using the formula for a_f for reducing the density of those fibrils corresponding to the angle μ_β and penalizing the corresponding adhesive traction ($k_1 = 1.1$). In this case, a minimum of the peeling force can be attained in correspondence of the selected value of μ_β.

The effect of the value of the standard deviation σ_β is shown in Fig. 8 for a test problem corresponding to $\mu_\beta = 45^\circ$. Based on this representation, the smaller σ_β, the higher the discrimination in maximizing or penalizing the interface cohesive traction in a certain direction. It is also observable that for the enhancing adhesion case and for a particular value of the r.m.s equal to $\sigma_\beta = 0.28$, the maximum peeling force exhibits a quasi plateau-like evolution for a certain range of the angle β, resulting in a minor discriminating effect due to σ_β.

2.2. Three-dimensional constitutive model

The previous two-dimensional model can be extended to three-dimensional problems by considering again an interface covered by fibrils adhering to one of the two surfaces of the interface and perfectly attached to the opposite one. By introducing a middle surface of the interface as the surface with average coordinates between those corresponding to the upper and lower sides of the two bodies, we define a local reference system characterized by two tangential vectors belonging to the middle surface, $\mathbf{t}_1$ and $\mathbf{t}_2$, and a normal vector $\mathbf{n}$. Fibrils are distributed over this middle surface depending on the middle surface in-plane angle θ, varying from 0 to 2π, and may have a different middle surface out-of-plane inclination β ranging from 0 to π, see Fig. 9.

In analogy with the two-dimensional case, we can introduce an adhesion factor $a_{f\beta}(\beta)$ related to the uniform or nonuniform distribution of fibrils depending on the angle β:

$$a_{f\beta}(\beta) = \begin{cases} 1, & \text{uniform distribution} \\ \frac{1}{\sigma_\beta\sqrt{2\pi}} \exp\frac{-(\beta-\mu_\beta)^2}{2\sigma_\beta^2}, & \text{nonuniform distr.} \end{cases} \tag{5}$$

Moreover, a second adhesion factor $a_{f\theta}(\theta)$ related to the distribution of fibrils in the plane of the middle surface can be similarly considered:

$$a_{f\theta}(\theta) = \begin{cases} 1, & \text{uniform distribution} \\ \frac{1}{\sigma_\theta\sqrt{2\pi}} \exp\frac{-(\theta-\mu_\theta)^2}{2\sigma_\theta^2}, & \text{nonuniform distrib.} \end{cases} \tag{6}$$

The latter adhesion factor plays an important role to distinguish between isotropic and anisotropic surface texturing. In paper tissue, for instance, the density of fibrils can be the same in all the in-plane directions as shown in Fig. 10, supporting the adoption of a uniform distribution. However, due machining of paper, a preferential alignment along a given direction may also take place and nonuniform distribution density functions would be better to represent real morphologies.

The overall adhesion factor $a_f(\beta,\theta)$ for three-dimensional problems is finally defined via the product between $a_{f\beta}(\beta)$ and $a_{f\theta}(\theta)$:

$$a_f(\beta,\theta) = \begin{cases} 1, & \text{uniform distribution} \\ a_{f\beta}a_{f\theta}, & \text{nonuniform distrib.} \\ \frac{k_1}{\sigma_\beta\sqrt{2\pi}}\frac{k_2}{\sigma_\theta\sqrt{2\pi}} - a_{f\beta}a_{f\theta}, & \text{nonuniform distrib. for detachment} \end{cases} \tag{7}$$

In analogy with the two-dimensional formulation, for each Mixed Mode condition represented by the components $g_{\rm loc,t1}, g_{\rm loc,t2}$ and $g_{\rm loc,n}$ of the relative displacement vector $\mathbf{g}_{\rm loc}$, we assume again that only the fibrils aligned along that direction are the primary fibrils transferring load. Under such an assumption, for a given relative displacement vector, the set of reacting fibrils will be defined by the angle θ computed as:

$$\theta(g_{\rm loc,t1}, g_{\rm loc,t2}) = \begin{cases} \arctan\left(\frac{g_{\rm loc,t2}}{g_{\rm loc,t1}}\right) & \text{if } g_{\rm loc,t1} \neq 0 \\ \pi/2, & \text{if } g_{\rm loc,t1} = 0 \end{cases} \tag{8}$$

and by the inclination angle β:

$$\beta(g_{\rm loc,t}, g_{\rm loc,n}) = \begin{cases} \arctan\left(\frac{g_{\rm loc,n}}{g_{\rm loc,t}}\right), & \text{if } \beta \geqslant 0, g_{\rm loc,t} \neq 0 \\ \pi/2, & \text{if } \beta \geqslant 0, g_{\rm loc,t} = 0 \\ \arctan\left(\frac{g_{\rm loc,n}}{g_{\rm loc,t}}\right) + \pi, & \text{if } g_{\rm loc,t} < 0 \end{cases} \tag{9}$$

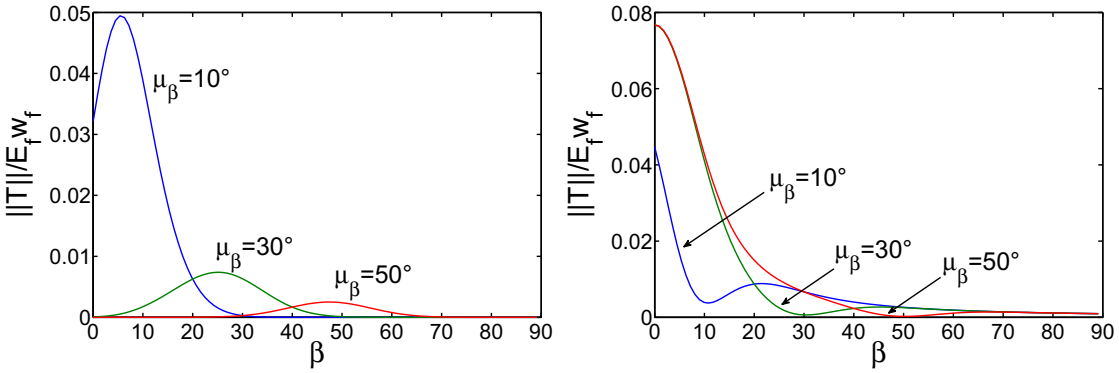

Fig. 7. Dimensionless maximum peeling force $\|\mathbf{T}\|/(E_f w_f)$ vs. peeling angle β for three different values of μ_β and for $\sigma_\beta = 0.14$ rad.

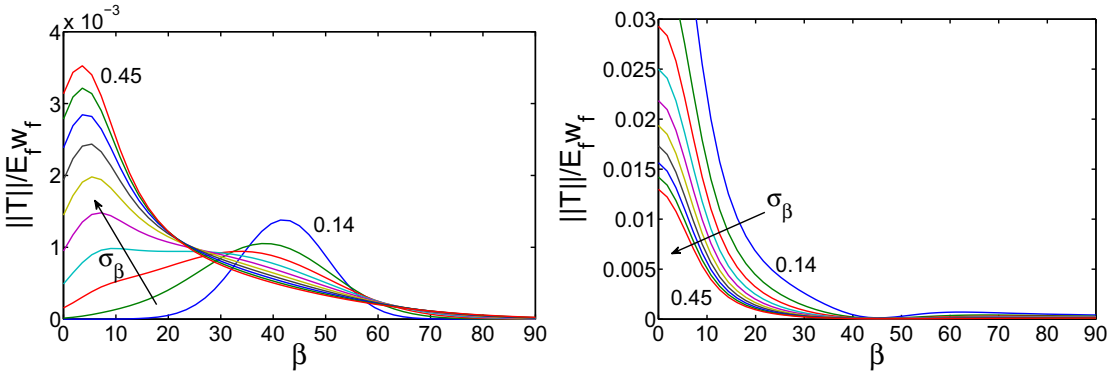

Fig. 8. Dimensionless maximum peeling force $\|\mathbf{T}\|/(E_f w_f)$ vs. peeling angle β depending on σ_β, for $\mu_\beta = 45°$.

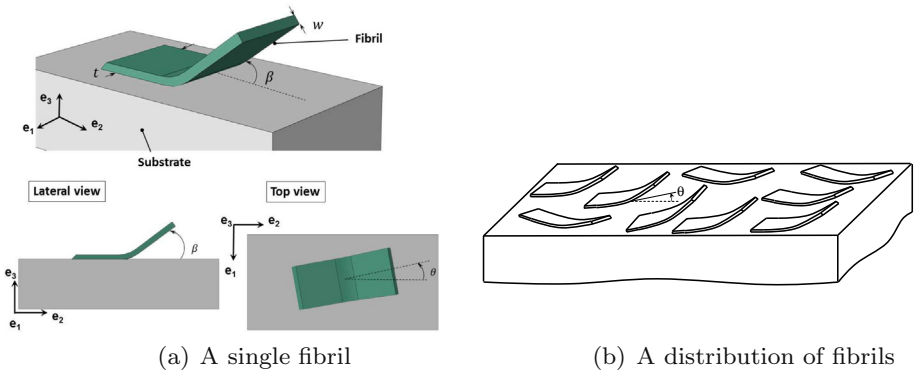

Fig. 9. (a) A sketch showing a single fibril and its orientation angles θ and β. (b) A sketch showing a collection of fibrils with different angles θ and β.

where $g_{\text{loc,t}} = \sqrt{g_{\text{loc,t1}}^2 + g_{\text{loc,t2}}^2}$ is the resultant tangential component of the relative displacement vector at the interface.

The peeling traction of each fibril is again provided by Eq. (4) as in the two-dimensional case, whereas its components in the local frame are:

$$T_{t1} = \|\mathbf{T}\| \frac{\lambda}{\|\mathbf{g}_{\text{loc,cr}}\|} \cos\beta \cos\theta \tag{10a}$$

$$T_{t2} = \|\mathbf{T}\| \frac{\lambda}{\|\mathbf{g}_{\text{loc,cr}}\|} \cos\beta \sin\theta \tag{10b}$$

$$T_n = \|\mathbf{T}\| \frac{\lambda}{\|\mathbf{g}_{\text{loc,cr}}\|} \sin\beta \tag{10c}$$

where $\lambda = \sqrt{g_{\text{loc,t}}^2 + g_{\text{loc,n}}^2}$ is the modulus of the total relative displacement vector.

In the case of an in-plane uniform distribution of fibrils, the cohesive traction vector $\|\mathbf{T}\|$ is dependent on β according to the peeling theory of an elastic tape as in the bi-dimensional case and it does not depend on the in-plane angle θ. However, in the most general case, adhesion can be selectively maximized or minimized in case of a combined in-plane and out-of-plane nonuniform distribution of fibrils.

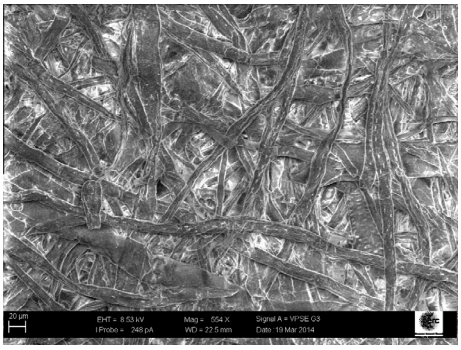

Fig. 10. Image of cellulose fibrils of paper tissue, showing a random orientation with almost a uniform distribution in the plane. The SEM image is taken under variable pressure conditions (VPSE sensor) at 8.5 kV, 554× magnification and a working distance of 22.5 mm.

3. Interface element formulation for large displacements

In applications regarding thin structural elements subjected to large displacements, such as biological membranes, paper sheets, viscoelastic materials for the encapsulation of solar cells, among many others, the complexity of their structural analyses relies on the fact that during the simulation the deformed configuration cannot be any longer approximated by the underformed one. In such scenarios, within the framework of cohesive models for delamination and debonding processes, the computation of the interface gap (global or projected over a local reference basis) according to the reference geometry can lead to errors depending upon the specific applications and materials tested. Large-displacement analyses require tracking of the surface separation, the relative rotations between the two sides of the interface and the simultaneous deformation of the two bodies separated by the interface.

In light of the previous arguments, large displacement interface element formulations have been proposed during the last decades. A pioneering attempt to solve this problem is due to Ortiz and Pandolfi (1999), who suggested the adoption of a reference middle surface of the cohesive element in the current configuration to define a convenient (deformed) surface for the calculation of the normal and tangential directions to the interface. Their formulation was particularized to a quadratic 3D interface element for matching tetrahedra.

In Qiu et al. (2001), an alternative formulation for a 2D interface element in large displacements was proposed by introducing a non symmetric co-variant reference system coincident with one of the two deformed sides of the interface. Other 2D and 3D novel formulations with emphasis on the problem of interface fibrilation were recently proposed in van den Bosch et al. (2007, 2008a). In this instance, the kinematics of the interface element was assumed to be similar to that corresponding to 2D or 3D trusses under large displacements and rotations.

In this study, a consistent interface element for large displacements is proposed for the implementation of the anisotropic cohesive law derived in Section 2. It represents an extension to three-dimensional problems of the two-dimensional formulation in Reinoso and Paggi (2014). The development of such a novel interface model is motivated by the notable geometric nonlinear effects that are evidenced in experimental studies with regard to failure analysis of fibril-based interfaces, see (Desai et al., 2011; Hoefnagels et al., 2010; Kramer and Berger, 1990). However, differently from other approximations using a global computation of the displacement gaps between the flanks of the interface and the subsequent evaluation of the cohesive law (van den Bosch et al., 2008a), a cohesive element relying on the midsurface definition is herein employed. This alternative approach is supported by the experimental evidence in Desai et al. (2011) for crazing of polymers where notable interface deformation but undergoing moderate rotations can be observed.

3.1. Interface element and FE formulation

This section concisely outlines the derivation of the large deformation interface element and the corresponding FE formulation for the 2D and 3D versions of the model.

Within the finite deformation setting, consider a pair of deformable bodies in the reference configuration $\mathscr{B}_0^{(1)}, \mathscr{B}_0^{(2)} \subset \mathbb{R}^n_{dim}$ (identified as Bulk-1 and Bulk-2 in Fig. 1), where $2 \leqslant n_{dim} \leqslant 3$ stand for the space dimension. Both bodies are subjected to the volume forces $\mathbf{F}_v^{(i)}$ with $i = 1, 2$, and the boundary conditions: $\mathbf{t}^i = \hat{\mathbf{t}}^i$ on $\partial\mathscr{B}^i_{0,\mathbf{t}}$ and $\mathbf{u}^i = \hat{\mathbf{u}}^i$ on $\partial\mathscr{B}^i_{0,\mathbf{u}}$ with $i = 1, 2$. Note that both deformable bodies might obey different constitutive laws within their own domains. The nonlinear deformation map $\boldsymbol{\varphi}(\mathbf{X}) : \mathbf{X} \to \mathbf{x}$ relating any material point in the reference configuration $\mathbf{X} \subset \mathscr{B}_0^{(i)}$ to the corresponding point in the current configuration $\mathbf{x} \subset \mathscr{B}_t^{(i)}$ at time $t \subset \mathbb{R}_+$ is introduced (see Fig. 1). The deformation gradient of the transformation, representing the linear map between the tangent vectors in the reference and in the current configurations is defined as: $\mathbf{F} := \partial_{\mathbf{X}}\varphi(\mathbf{X}, t)$, with the Jacobian $J = \det[\mathbf{F}] > 0$ and $\partial_{\mathbf{X}}$ denoting the partial derivative with respect to the reference frame. The interface between both arbitrary bodies $S_0 \subset \mathbb{R}^{n_{dim}-1}$ in the reference configuration ($s_0 \subset \mathbb{R}^{n_{dim}-1}$ in the current configuration) is assumed to be characterized by the micromechanical fibril-based cohesive law comprehensively described in Section 2, for 2D and 3D applications, see Fig. 1.

The weak form of the contribution of the interface to the Principle of Virtual Work of the complete system reads:

$$\delta\Pi_{\text{intf}}(\mathbf{u}, \delta\mathbf{u}) = \delta\mathbf{u}^{\mathrm{T}}\left[\int_{S_0}\left(\frac{\partial\mathbf{g}_{\text{loc}}}{\partial\mathbf{u}}\right)^{\mathrm{T}}\mathbf{T}\mathrm{d}S\right], \quad \forall\delta\mathbf{u} \in \mathscr{V} \tag{11}$$

where $\mathbf{g}_{\text{loc}}$ is the gap vector that accounts for relative opening and sliding between the two flanks of the interface and represents the work conjugated magnitude to the cohesive tractions, and $\delta\mathbf{u} \in \mathscr{V}$ denotes the kinematically admissible virtual displacements. Note that in such geometrically nonlinear procedure, the traction vector acting within the interface in Eq. (11) regards the Piola–Kirchhoff traction vector that is defined in the reference configuration.

The updated coordinates of a generic point are given by $\mathbf{x} = \mathbf{X} + \mathbf{u}$. In case of moderate rotations, it is convenient to introduce a middle surface (in 3D) or a middle line (in 2D) of the interface in the updated configuration by averaging the position vectors and displacement fields of the upper and lower faces (in 3D) or sides (in 2D) of the interface, see Fig. 11. Hence, the position vector $\overline{\mathbf{x}}$ of a generic point along this middle surface/line can be determined by pre-multiplying the positioning vector $\mathbf{x}$ by an averaging operator $\mathbf{M}$, whereas its discretized version $\overline{\mathbf{x}}^e$ can be obtained complying with the isoparametric concept using the operator $\mathbf{N}$ that collects the shape functions:

$$\overline{\mathbf{x}} = \mathbf{M}\mathbf{x}; \quad \overline{\mathbf{x}}^e = \mathbf{N}\mathbf{M}\mathbf{x}^n, \tag{12}$$

where the superscript n denotes quantities evaluated at the nodes of the discretized system. The operator $\mathbf{N}$ is as customary defined in the local parametric space ranging: (i) 2D $\xi \in [-1, 1]$, where η is the natural coordinate, and (ii) 3D $\{\xi, \eta\} \in [-1, 1] \times [-1, 1]$, where ξ, η identify the natural coordinates defined in the middle surface of the element in the three-dimensional version.

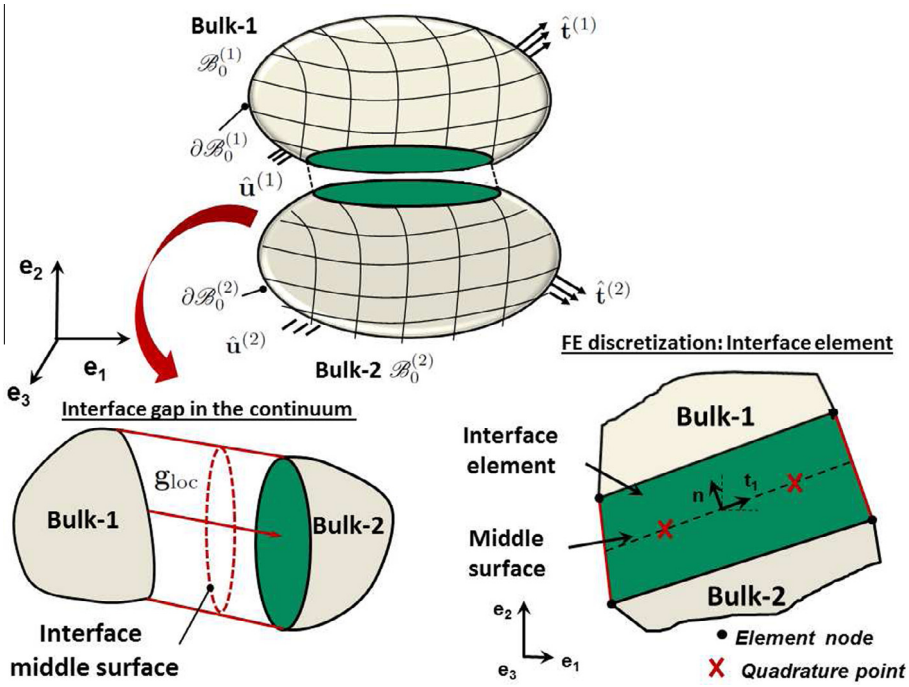

Fig. 11. A sketch of the interface element.

Similarly, the coordinates of the points belonging to the middle surface/line in the reference configuration, $\overline{\mathbf{X}}$, and their displacement vector, $\overline{\mathbf{u}}$, can be computed via a standard interpolation procedure from the nodal quantities as follows:

$$\overline{\mathbf{X}} \cong \overline{\mathbf{X}}^e = \mathbf{N}\mathbf{M}\mathbf{X}^n, \quad \overline{\mathbf{u}} \cong \overline{\mathbf{u}}^e = \mathbf{N}\mathbf{M}\mathbf{d} \tag{13}$$

where $\mathbf{X}^n$ and $\mathbf{d}$ denote, respectively, the position vector of the nodes in the reference system and their nodal displacement vector.

The gap vector in the reference Cartesian frame, $\mathbf{g}$, can be obtained by pre-multiplying the nodal displacement vector $\mathbf{d}$ by a suitable operator $\mathbf{L}$ which provides the difference between the displacements of the upper and the lower bodies at the interface. Within the FE discretization, the interpolation scheme of the gap vector reads:

$$\mathbf{g} \cong \mathbf{g}^e = \mathbf{N}\mathbf{L}\mathbf{d} \tag{14}$$

The constitutive relation for the interface, i.e., the so-called cohesive zone model (CZM), is provided in the local frame. Therefore, the gap vector in this local frame, $\mathbf{g}_{\text{loc}}$, has to be computed by multiplying the gap vector in the reference frame by a rotation operator $\mathbf{R}$:

$$\mathbf{g}^e_{\text{loc}} = \mathbf{R}(\mathbf{u})\mathbf{g}^e \tag{15}$$

The rotation operator is computed through the definition of the local setting in which the cohesive law is evaluated, see Appendix. Note that, in case of large displacements, the operator $\mathbf{R}(\mathbf{u})$ is a function of the displacement field. As a consequence of this dependency, the linearization of the virtual work contribution of the interface element (11) for the application of the Newton–Raphson solution procedure leads to the so-called geometric stiffness matrix.

Inserting the discretization scheme described above, the virtual variation of gaps in Eq. (11) takes the form

$$\frac{\partial \mathbf{g}_{\text{loc}}}{\partial \mathbf{u}} \cong \frac{\partial \mathbf{g}^e_{\text{loc}}}{\partial \mathbf{d}} = \mathbf{R}\mathbf{N}\mathbf{L} + \frac{\partial \mathbf{R}}{\partial \mathbf{d}}\mathbf{N}\mathbf{L}\mathbf{d} = \mathbf{R}\mathbf{B} + \frac{\partial \mathbf{R}}{\partial \mathbf{d}}\mathbf{B}\mathbf{d} \tag{16}$$

where the differentiation of the second order tensor $\mathbf{R}$ with respect to the components of the vector $\mathbf{d}$ leads to a third order tensor (Reinoso and Paggi, 2014). To simplify the notation, the operator $\mathbf{B} = \mathbf{N}\mathbf{L}$ has been introduced in Eq. (16).

The discretized version of Eq. (11) leads to the following general formulation:

$$\begin{aligned}\delta\Pi^e_{\text{int}}(\mathbf{d},\delta\mathbf{d}) &= \delta\mathbf{d}^{\mathrm{T}}\left[\int_{S_0}\left(\mathbf{R}\mathbf{B}+\frac{\partial \mathbf{R}}{\partial \mathbf{d}}\mathbf{B}\mathbf{d}\right)^{\mathrm{T}}\mathbf{T}\,\mathrm{d}S\right] \\ &= \delta\mathbf{d}^{\mathrm{T}}\left[\mathbf{f}^e_{\text{int}}\right], \quad \forall\delta\mathbf{d}\in\mathscr{V}^h\end{aligned} \tag{17}$$

where the vector $\delta\mathbf{d}\in\mathscr{V}^h$ stands for the kinematically admissible virtual nodal displacements, and $\mathbf{f}^e_{\text{int}}$ identifies the internal force vector at the element level corresponding to the interface. The linearization of Eq. (17) at the element level renders

$$\begin{aligned}\Delta\delta\Pi^e_{\text{int}}(\mathbf{d},\delta\mathbf{d},\Delta\mathbf{d}) &= \delta\mathbf{d}^{\mathrm{T}}\left\{\int_{S_0}\mathbf{B}^{\mathrm{T}}\mathbf{R}^{\mathrm{T}}\mathbf{C}\mathbf{R}\mathbf{B}\,\mathrm{d}S+\int_{S_0}\left[2\mathbf{B}^{\mathrm{T}}\frac{\partial \mathbf{R}^{\mathrm{T}}}{\partial \mathbf{d}}\mathbf{T}+\mathbf{d}^{\mathrm{T}}\mathbf{B}^{\mathrm{T}}\frac{\partial \mathbf{R}^{\mathrm{T}}}{\partial \mathbf{d}}\mathbf{C}\frac{\partial \mathbf{R}}{\partial \mathbf{d}}\mathbf{B}\mathbf{d}\right.\right. \\ &\quad\left.\left.+\left(\mathbf{B}^{\mathrm{T}}\mathbf{R}^{\mathrm{T}}\mathbf{C}\frac{\partial \mathbf{R}}{\partial \mathbf{d}}\mathbf{B}\mathbf{d}+\mathbf{d}^{\mathrm{T}}\mathbf{B}^{\mathrm{T}}\frac{\partial \mathbf{R}^{\mathrm{T}}}{\partial \mathbf{d}}\mathbf{C}\mathbf{R}\mathbf{B}\right)\right]\mathrm{d}S\right\}\Delta\mathbf{d} \\ &= \delta\mathbf{d}^{\mathrm{T}}\left[\mathbf{K}_{\text{mat}}+\mathbf{K}_{\text{geom}}\right]\Delta\mathbf{d}\end{aligned} \tag{18}$$

where $\mathbf{C}$ stands for the constitutive tangent tensor, that is derived in detail in Section 3.2, and the integral terms $\mathbf{K}_{\text{mat}}$ and $\mathbf{K}_{\text{geom}}$ are the element material and geometrical stiffness matrices, respectively, see Reinoso and Paggi (2014) for further details in the derivation.

In addition, it is worth mentioning that the formulation is further enhanced by a penalty stiffness k that is used to avoid interpenetration between the two opposite flanks of the interface (Balzani and Wagner, 2008). Note that this contact condition requires the decomposition of the gaps into normal and tangential components, as performed here. Alternative formulations based on the global evaluation of the cohesive law also need this decomposition, as discussed in van den Bosch et al. (2008a). This process yields to the modification of the traction vector and the

corresponding consistent tangent operator, which include an additional contribution referred to their normal component in case the contact condition is invoked.

3.2. Interface consistent tangent operator

The consistent tangent operator plays a key role in fully implicit FE formulations and it is computed via the consistent linearization of the discretized form of the traction vector $\mathbf{T}$, namely $\mathbf{C} = \partial\mathbf{T}/\partial\mathbf{d}$. According to the traction vector definition relying on the Kendall peeling theory, see Eq. (4), the linearization of $\mathbf{T}$ takes the general form

$$\Delta\mathbf{T} = \Delta\left[a_f\mathbf{t}\right] = \Delta a_f\mathbf{t} + a_f\Delta\mathbf{t} \tag{19}$$

where Δ stands for linearization with respect to $g_{\mathrm{loc,t}}$ or to $g_{\mathrm{loc,n}}$. In the 2D case, the adhesion factor depends upon the angle β, whereas in the 3D version of the model this factor becomes function of the angles β and θ. Moreover, as these angles are updated along the deformation process to account for the geometrical effects, the adhesion factor needs to be accordingly linearized with respect to the kinematic field as expressed in Eq. (19). However, in case of a uniform distribution we have $a_f = 1$ and $\Delta a_f = 0$.

3.2.1. Two-dimensional fibril-based consistent tangent operator

The normal and tangential components of the 2D version of the proposed fibril-based interface model, which only depends on the angle β, are given in Eq. (4). The consistent linearization of such components with respect to the normal and tangential gaps are:

$$\Delta T_t = \Delta\left[a_f(\beta)\mathbf{t}(\beta)\right]\frac{\lambda}{\|\mathbf{g}_{\mathrm{loc,cr}}\|}\cos\beta + a_f(\beta)\mathbf{t}(\beta)\Delta\left[\frac{\lambda}{\|\mathbf{g}_{\mathrm{loc,cr}}\|}\right]\cos\beta + a_f(\beta)\mathbf{t}(\beta)\frac{\lambda}{\|\mathbf{g}_{\mathrm{loc,cr}}\|}\Delta[\cos\beta] \tag{20}$$

$$\Delta T_n = \Delta\left[a_f(\beta)\mathbf{t}(\beta)\right]\frac{\lambda}{\|\mathbf{g}_{\mathrm{loc,cr}}\|}\sin\beta + a_f(\beta)\mathbf{t}(\beta)\Delta\left[\frac{\lambda}{\|\mathbf{g}_{\mathrm{loc,cr}}\|}\right]\sin\beta + a_f(\beta)\mathbf{t}(\beta)\frac{\lambda}{\|\mathbf{g}_{\mathrm{loc,cr}}\|}\Delta[\sin\beta] \tag{21}$$

It is worth noting that all of the derivatives in (20) and (21) involve simple trigonometric and polynomial functions, and therefore their final results are omitted here for the sake of brevity. The material tangent stiffness matrix is arranged as follows

$$\mathbf{C} = \begin{bmatrix} \frac{\partial T_t}{\partial g_{\mathrm{loc,t}}} & \frac{\partial T_t}{\partial g_{\mathrm{loc,n}}} \\ \frac{\partial T_n}{\partial g_{\mathrm{loc,t}}} & \frac{\partial T_n}{\partial g_{\mathrm{loc,n}}} \end{bmatrix} \tag{22}$$

3.2.2. Three-dimensional fibril-based consistent tangent operator

With regard to the 3D version of the fibril-based interface model, the linearization of the traction vector becomes rather more complex due to the sequence of factors dependent upon the kinematic field, see Eq. (10). Note also that, as was addressed above, the adhesion factor is a function of β and θ, whose linearization is expanded as follows: $\Delta a_f = \Delta\left[a_{f\beta}(\beta)\right]a_{f\theta}(\theta) + a_{f\beta}(\beta)\Delta\left[a_{f\theta}(\theta)\right]$. Relying on the traction definition formerly derived in Eq. (10), the linearization of the normal and of the two tangential components can be expressed as

$$\Delta T_{t1} = \Delta\left[a_f(\beta,\theta)\mathbf{t}(\beta)\right]\frac{\lambda}{\|\mathbf{g}_{\mathrm{loc,cr}}\|}\cos\beta\cos\theta + a_f(\beta,\theta)\mathbf{t}(\beta)\Delta\left[\frac{\lambda}{\|\mathbf{g}_{\mathrm{loc,cr}}\|}\right] \times \cos\beta\cos\theta + a_f(\beta)\mathbf{t}(\beta)\frac{\lambda}{\|\mathbf{g}_{\mathrm{loc,cr}}\|}(\Delta[\cos\beta]\cos\theta + \cos\beta\Delta[\cos\theta]) \tag{23a}$$

$$\Delta T_{t2} = \Delta\left[a_f(\beta,\theta)\mathbf{t}(\beta)\right]\frac{\lambda}{\|\mathbf{g}_{\mathrm{loc,cr}}\|}\cos\beta\sin\theta + a_f(\beta,\theta)\mathbf{t}(\beta)\Delta\left[\frac{\lambda}{\|\mathbf{g}_{\mathrm{loc,cr}}\|}\right] \times \cos\beta\sin\theta + a_f(\beta)\mathbf{t}(\beta)\frac{\lambda}{\|\mathbf{g}_{\mathrm{loc,cr}}\|}(\Delta[\cos\beta]\sin\theta + \cos\beta\Delta[\sin\theta]) \tag{23b}$$

$$\Delta T_n = \Delta\left[a_f(\beta,\theta)\mathbf{t}(\beta)\right]\frac{\lambda}{\|\mathbf{g}_{\mathrm{loc,cr}}\|}\sin\beta + a_f(\beta,\theta)\mathbf{t}(\beta)\Delta\left[\frac{\lambda}{\|\mathbf{g}_{\mathrm{loc,cr}}\|}\right] \times \sin\beta + a_f(\beta,\theta)\mathbf{t}(\beta)\frac{\lambda}{\|\mathbf{g}_{\mathrm{loc,cr}}\|}\Delta[\sin\beta] \tag{23c}$$

Finally, the tangent operator for the interface constitutive relation reads

$$\mathbf{C} = \begin{bmatrix} \frac{\partial T_{t1}}{\partial g_{\mathrm{loc,t1}}} & \frac{\partial T_{t1}}{\partial g_{\mathrm{loc,t2}}} & \frac{\partial T_{t1}}{\partial g_{\mathrm{loc,n}}} \\ \frac{\partial T_{t2}}{\partial g_{\mathrm{loc,t1}}} & \frac{\partial T_{t2}}{\partial g_{\mathrm{loc,t2}}} & \frac{\partial T_{t2}}{\partial g_{\mathrm{loc,n}}} \\ \frac{\partial T_n}{\partial g_{\mathrm{loc,t1}}} & \frac{\partial T_n}{\partial g_{\mathrm{loc,t2}}} & \frac{\partial T_n}{\partial g_{\mathrm{loc,n}}} \end{bmatrix} \tag{24}$$

It is remarkable that, similarly to the previous 2D case, the derivatives of the functions involved are rather simple. However, again, the dependence of both β and θ upon the current configuration makes these derivations quite lengthy operations. The 2D and 3D versions of the large deformation interface element and the cohesive law have been implemented as user elements in the FE program FEAP (Zienkiewicz and Taylor, 2004).

4. Model parameters identification

The cohesive zone model herein proposed is based on the adhesion theory of an elastic tape (Kendall, 1975) used as a constitutive law for each fibril. According to Eq. (12), it requires the identification of the following parameters: the Young modulus of the fibrils, E_f, their width, w_f, the adhesion energy, G, and the out-of-plane thickness of the fibril, t. A suitable approach to identify all these model parameters is to perform an experimental test with a tensile stage inside a chamber of a scanning electron microscope (SEM) to observe the evolution of the morphology of microscopical fibrils during the deformation process. For instance, single edge-notched rectangular specimens made of a polystyrene film have been tested under tension in Desai et al. (2011). Crazing in form of fibrils with a very regular pattern aligned with the Mixed Mode deformation angle have been observed (see Fig. 5(b)). Apart from the Young modulus of the fibrils that can be selected as the bulk modulus of polystyrene ($E_f = 3.5$ GPa), SEM images allow an easy identification of the geometrical parameters. The width w_f is approximately equal to 80 nm and the out-of-plane thickness can be set equal to 800 nm, i.e., the film thickness. Desai et al. (2011) proposed also a method to determine the traction-separation curve by differentiating the experimentally computed J-integral as a function of the crack-tip opening that was directly measured from SEM images. The obtained traction-separation relation, accounting for all the stages of crazing from void formation up to fibril failure, is shown in Fig. 12. The curve is almost linear in the ascending branch due to the elastic elongation of the fibrils, up to a peak cohesive traction. Afterwards, softening takes place due to the abrupt failure of fibrils. In our formulation, a tension cut-off has been assumed, which, albeit an approximation, it is not too far from the experimental response. In particular, a critical crack opening displacement $\|g_{\mathrm{loc,cr}}\| = 18$ μm and an adhesion energy $G = 60$ N/μm have been used to obtain the traction-separation law shown in Fig. 12 with solid blue line, which is a reasonable approximation of the experimental data reported with black bullets in the same figure.

Regarding the coefficient $a_f(\beta)$, the phenomenon of re-orientation of the fibrils during the deformation process to maintain $\beta = \psi$ (see Fig. 5(b)) suggests the use of $a_f(\beta) = 1$ as previously discussed for the particular case of crazing failure.

In case of cellulose fibers, micro-mechanical testing facilities can again provide most of the information related to the geometrical parameters of the fibrils, see Fig. 5(a). The in-plane distribution function $a_f(\theta)$ can also be experimentally determined from SEM images of the surface of paper tissue as Fig. 10. Regarding mechanical testing, double cantilever beam tests can be performed by adapting the standard tensile tester as shown in Fig. 14. In this case, the traction-separation law can be determined from the global force–displacement curves by following the procedure suggested by Desai et al. (2011) and taking into account the different specimen geometry.

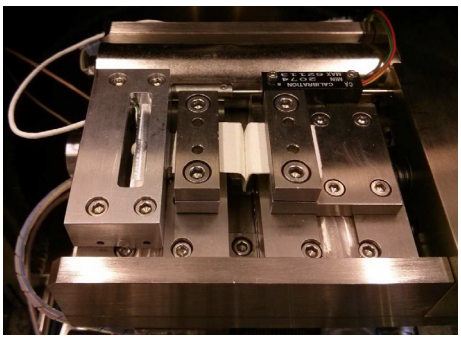

Fig. 13. Setup of a double cantilever beam test on layered paper performed with a tensile stage inside a SEM.

5. Representative applications of technological interest concerning anisotropic interfaces

As shown in Section 2, the proposed cohesive zone model is highly anisotropic as a result of the dependency of the peeling force on the angle β according to Kendall's theory and of the adhesion factor taking into account the nonuniform distribution of the density of fibrils with different inclination. These features can be suitably exploited in order to realize functional adhesives and interfaces for specific applications. In this section we address two possible examples of technological interest where the present computational model can provide useful hints for better design of adhesives and understanding the anisotropic behavior of fibrillar interfaces.

The first example regards the analysis an innovative adhesive layer whose microstructure might be designed to facilitate debonding between glass and substrate in photovoltaic modules. This can be very effective for making easier recycling operations, see Section 5.1. The second application concerns with the interpretation of the effect of cellulose fibers orientation on the mechanical bonding between paper tissues, see Section 5.2.

5.1. Enhancement of cover-encapsulant debonding in innovative photovoltaic modules for recycling purposes

Photovoltaic (PV) modules available on the market are manufactured through a layered structure which is generally composed of: (i) a very thin backsheet of about 0.1 mm; (ii) an encapsulant layer of 0.5 mm; (iii) a layer of silicon solar cells 0.16 mm thick; (iv) another encapsulant layer of 0.5 mm; and finally (v) a cover made either of a plastic material or, more frequently, a thick glass cover of 4.5 mm for environmental protection (see Paggi et al. (2013, 2014) for more details). Apart from an enhanced resistance to cracking and to increase the module electric performance and durability (Paggi et al., 2013), a new generation of PV modules should be easier to recycle. At present, in case of a PET cover, it is possible to disassemble the PET material from the rest of the cell just by warming up the cover surface at about 100°C and peeling it off. The adhesive experiences crazing contributing to progressive delamination, see a sequence in Fig. 12. In case of a thick glass cover, this type of controlled peeling is difficult to be realized and thermal treatments of the whole PV module up to 600°C is necessary to separate the components. Based on these arguments, a design of an innovative encapsulant layer with enhanced crazing along a specific direction of pulling would be very useful for recycling.

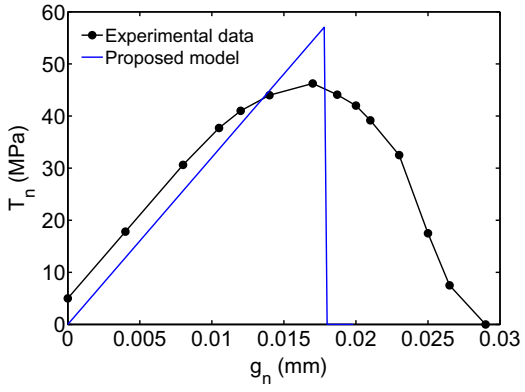

Fig. 12. Traction-separation relation for a fibrillar interface due to crazing in polystyrene: experimental data from Desai et al. (2011) and model approximation.

Although not yet realized in practice, the theory in Section 2 can be exploited by designing an encapsulant interface such that adhesion is minimized in correspondence to a certain peeling angle $\overline{\beta}$, let say 45° for exemplary purposes. A possibility to realize a minimum adhesion at a certain angle is to act on the distribution function of the fibrils that must provide a minimum density in correspondence of that angle. An option could be to bond with a polymeric adhesive two surfaces with a rough texture designed in such a way that crazes form with an initial inclination dependent on the rough texture, as it happens in case of the local contact angle between the fibrils of a Gecko's spatula on a rough surface, see Fig. 3.

Let assume for instance a Gaussian distribution of fibrils having a minimal density at $\mu_\beta = \overline{\beta}$ and with a given r.m.s., e.g., $\sigma_\beta = 0.45$. In this way, the maximum peeling force of the fibril will present a minimum in correspondence of μ_β. For this application, a homogeneous distribution of fibrils in the plane is considered, so that we can simply use the 2D formulation and perform numerical simulations under the assumption of plain strain conditions.

We therefore simulate a peeling test of a thin laminate 0.26 mm thick composed of backsheet, silicon and the encapsulant from a thick glass 4.5 mm thick. The lateral size is 30 mm and the out of plane thickness is 1 mm. The material parameters for those materials are summarized in Paggi et al. (2013) and are: Young's modulus of glass equal to 73 GPa, Young's modulus of silicon equal to 130 GPa, Young modulus of the EVA fibrils equal to 20 MPa, adhesion energy equal to 500 N/mm, Poisson ratios equal to 0.2. The geometrical parameters of the fibrils are $w_f = 1$ μm, the critical crack opening is set equal to 1 mm, and the length of the fibrils is 1 mm. The simulation is carried out under plane strain conditions. A penalty parameter $k = 1 \times 10^5$ N/mm^2 has been included to avoid interpenetration in the contact regions along the interface. The numerical test is performed by considering large deformation hyperelastic material models for the continuum (wall) elements.

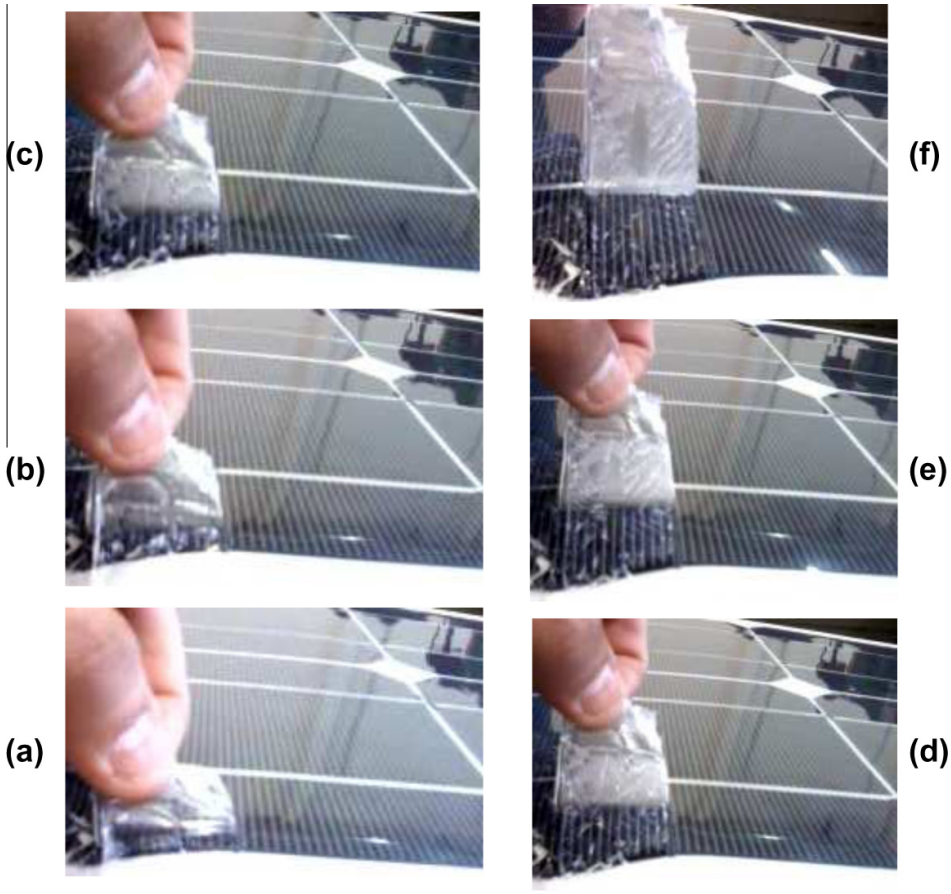

Fig. 14. Different sequences of debonding between a plastic cover and the encapsulant of solar cells.

The present large displacement interface element formulation is used to discretize the interface with 300 finite elements, allowing for a consistent coupling with the continuum elements. According to the sketches given in Fig. 15, the boundary conditions are clamped supports on the lower side of the specimen and on the left hand side. A prescribed displacement to the node located at the right edge of the upper layer is imposed. The simulations are therefore carried out under displacement control and different angles α are considered for the imposed displacement (pulling direction) as shown in the respective sketches in Figs. 15(d), whereas Fig. 15(a) depicts the variation of the maximum peeling force with respect to the peeling angle for a single fibril.

In this problem, the response of the interface will strongly depend on the rotation of the middle line of the interface elements and we expect to have a very weak response and easy delamination when the local peeling angle β approaches 45°. The correlation between the angle α and the angle β which varies along the interface and with the time step is not trivial since it depends on the displacement field and the relationship eventually varies from point to point along the interface. From the numerical results we observe that the interface achieves a maximum peeling force F of about 2 N in case of $\alpha = 45°$ (Fig. 15(b)). This peeling force is significantly decreased in case of $\alpha = 90°$, which is a loading condition leading to a local peeling angle proximal to $\beta \cong 45°$ along the interface elements (Fig. 15(c)). A further increase of α up to 104° leads to local peeling angles larger than 45° and therefore an increase in the peeling force F (Fig. 15(d)). These results are in line with the maximum peeling force for a single fibril with respect to the peeling angle (Fig. 15(a)), in which the minimum value of this force was obtained for 45°. Additionally, it is worth mentioning that the post-peak evolution response notably depends on the peeling angle. Thus, a quasi-brittle post-peak evolution of the interface is obtained for $\beta = 45°$, whereas a clear softening branch takes place for the other cases examined ($\beta = 45°$ and $\beta = 104°$).

Based on the previous discussion, this example shows that disassembling can be highly facilitated and controlled by using a nonuniform distribution of fibrils with their minimum density in correspondence of $\mu_\beta = 45°$. The local angle $\beta = \psi$ along the interface is shown in Fig. 16 for different values of α.

5.2. Understanding fibril actions in the mechanical joining of paper layers

The second exemplary problem investigated in this work regards the understanding of adhesion between paper tissues. Thin layers of paper can be efficiently joined without glue by wetting their common interface and exerting a localized pressure (see, e.g., an image of the joint in Fig. 13). In this process, due to the anisotropy of paper caused by a preferred alignment of cellulose fibrils along the machining direction, the adhesive force of the joint is expected to be different in two orthogonal directions. Preliminary peeling tests conducted in the Multi-scale Analysis of Materials laboratory of the IMT Institute for Advanced Studies Lucca have revealed that the required peeling force for the detachment of a double cantilever beam specimen oriented along the fibrils direction can be higher than that obtained with the fibrils oriented along the orthogonal direction. These experimental observations motivate the analysis of such applications with the aim of having a closer insight into the micro-mechanical phenomena that

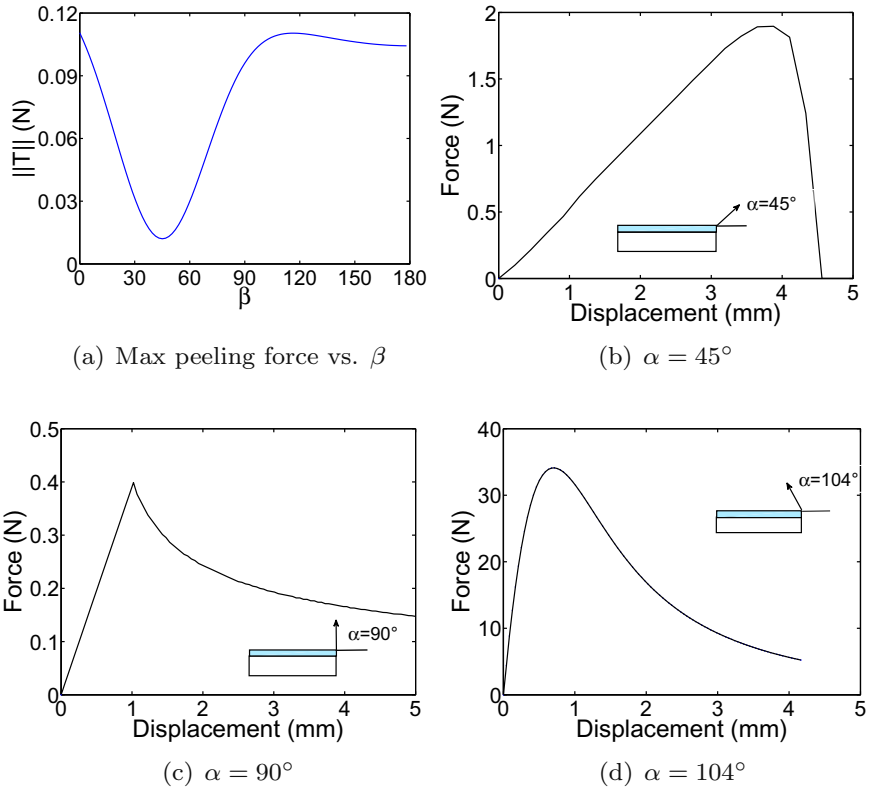

(a) Max peeling force vs. β (b) $\alpha = 45°$

(c) $\alpha = 90°$ (d) $\alpha = 104°$

Fig. 15. (a) Maximum peeling force with respect to the inclination angle β of a single fibril. Load displacement evolution curves for peeling applications using different values of the pulling angle α: $\alpha = 45°$ (b), $\alpha = 90°$ (c) and $\alpha = 104°$ (d).

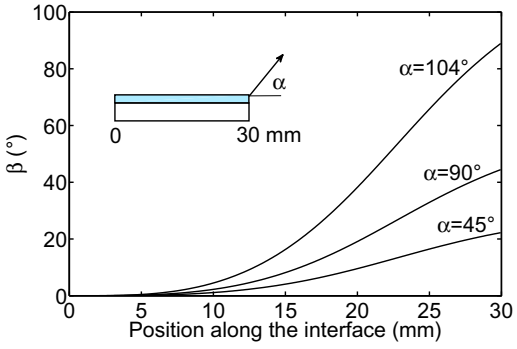

Fig. 16. Local angle $\beta = \psi$ along the interface for different values of the external load angle α. Force displacement curves are shown in Fig. 15.

take place in such interfaces. In particular, this applications require the use of the 3D formulation of the anisotropic CZM herein proposed since it is important to take into account the machining direction effect which affects the in-plane orientation of the fibrils. Moreover, the present formulation provides a consistent way to account for the effect of fibril anisotropy on the cohesive zone model response.

A sketch of the double cantilever beam test geometry is shown in Fig. 17. We consider a thin structure composed of two joined 10×10 mm paper sheets with 0.125 mm thickness each. The supporting conditions are those typical for a double cantilever beam (DCB) test where, referring to the representation given in Fig. 17, the left side is fully clamped whereas opening vertical displacements of opposite sign are imposed to all the nodes belonging to the outer edges on the right. These sheets are discretized by 50 linear 8-noded brick finite elements per side and separated by 3D interface elements for large displacements. An initial notch 2 mm long is considered. The parameters used for the CZM are $E_f = 2$ GPa, $w = t = 0.1$ μm, $\|\mathbf{g}_{loc,cr}\| = 10$ μm, $G = 0.01$ N mm. We consider an anisotropic distribution of fibrils in the plane with a maximum frequency in correspondence either of $\mu_\theta = 0°$ (aligned along the testing direction) or at $\mu_\theta = 90°$ (orthogonal to the testing direction). The distribution of fibrils inclinations is centered at $\mu_\beta = 0°$ in both cases and we assume standard deviations $\sigma_\theta = \sigma_\beta = 2$ for both distributions, to model a weak anisotropy. The resulting maximum peeling force in the two case studies is shown in Fig. 18.

The result of the numerical simulations in terms of total peeling force F vs. crack mouth opening displacement (CMOD) for the two case studies is shown in Fig. 19, where a clear effect of the anisotropic distribution of fibrils is evidenced in terms of the peak peeling force between the two cases herein examined. Thus, in line with the preliminary testing results previously mentioned, the effect of the main value of the fibrils orientation is clearly observed, exhibiting a higher maximum peeling force for $\mu_\theta = 0°$ than that corresponding to $\mu_\theta = 90°$ (with a factor about 1.2 between the peak forces predicted). This effect is fundamentally attributed to the consideration of $a_{f\theta}$ into the computation of the total adhesion factor a_f. Thus, in case the in-plane fibril angle is set to $\mu_\theta = 0°$, the external actions is aligned with the main resistance direction and corresponding to the maximum density of fibrils (see Fig. 18(a)), due to the fact that the principal load bearing mechanism of the fibrils is assumed to correspond to axial loading. In contrast to this, in case $\mu_\theta = 90°$, the peeling actions imposed to the specimen ($\theta = 0°$) are deviated with respect to direction of maximum density of fibrils (that is $\mu_\theta = 90°$, see Fig. 18(b)). Therefore, the load bearing capacity of the interface is not fully optimized and the obtained peak load is lower than that corresponding to the precedent loading scenario herein analyzed. The slightly smoother transition at the peak load in case of $\theta = 90°$ than for $\theta = 0°$ is due to the smoother variability of the modulus of the

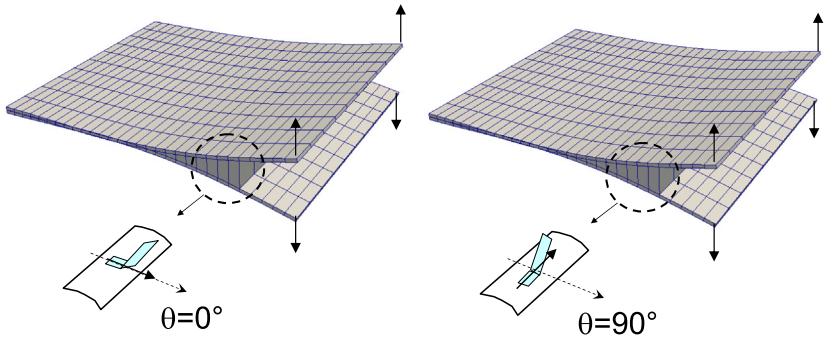

Fig. 17. Sketch of the peeling test and in-plane anisotropic distribution of fibrils: (a) Gaussian distribution with mean value $\mu_\theta = 0^\circ$ (alignment with the testing direction); (b) Gaussian distribution with mean value $\mu_\theta = 90^\circ$ (orthogonal to the testing direction).

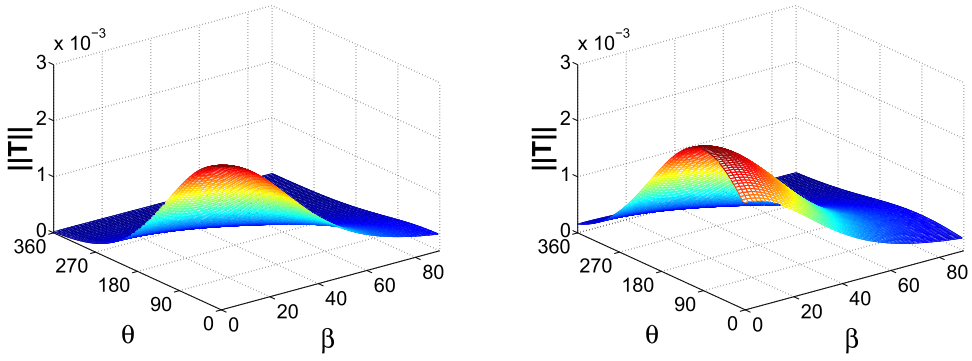

(a) Max density of fibrils aligned with the testing direction, $\mu_\theta = 0^\circ$

(b) Max density of fibrils orthogonal with the testing direction, $\mu_\theta = 90^\circ$

Fig. 18. Maximum peeling force $\|T\|$ vs. peeling angle β and in-plane angle θ for $\mu_\beta = 0^\circ$, $\sigma_\beta = \sigma_\theta = 2$ and (a) $\mu_\theta = 0^\circ$ or (b) $\mu_\theta = 90^\circ$.

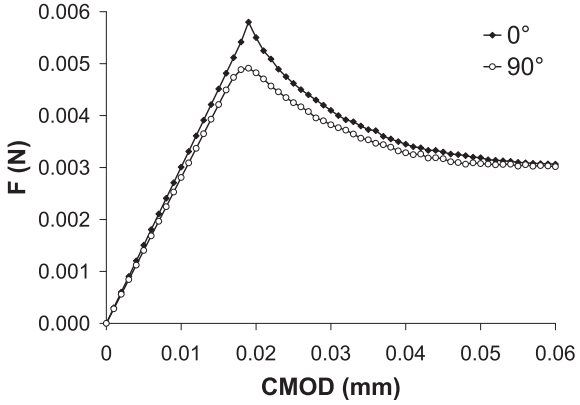

Fig. 19. Peeling force vs. crack mouth opening displacement for the two different CZM relations in Fig. 18 corresponding to testing joined paper tissues in the preferred direction of fibers inclination, $\mu_\theta = 0^\circ$, or orthogonal to the processing direction, $\mu_\theta = 90^\circ$.

maximum traction vector $\|\mathbf{T}\|$ with β which is changing along the interface during the evolution of the delamination process. For a comparison of these trends, please see Fig. 19. Nevertheless, note that once the decohesion process starts (the *F*-CMOD post-peak evolution), both structured interfaces tend asymptotically to the same final value, evidencing again the remarkable role that the relation between the peeling and the fibril orientation directions plays in decohesion.

6. Conclusion and outlook

In the present paper, a new anisotropic cohesive zone model for fibrillar microstructured interfaces undergoing large deformations has been proposed. The idea was to consider a distribution of fibrils with different in-plane and out-of-plane (peeling) orientations, each one obeying to the Kendall's peeling theory. The resulting traction-separation relation has been determined by assuming that only the fibrils with an orientation β equal to the Mixed Mode deformation angle ψ are contributing to the load transfer. Moreover, a density distribution function of fibrils dependent on the angle β has been taken into account as a penalization factor. This model allows simulating two possible scenarios observed in case of fibrillar interfaces: (i) the action of cellulose fibrils joining paper tissues, and (ii) the re-orientation mechanism of crazes in polymers.

Moreover, acting on the adhesion factor to modify the spatial density of fibrils depending on their orientations, it has been shown that adhesion or decohesion can be suitably enhanced along specific angles. The spatial distribution of fibrils orientation provides therefore a possible explanation to the anisotropic adhesive response of natural systems, alternative to the explanation based on the effect of a bulk anisotropy proposed in Yao and Gao (2006). It is worth mentioning that the present model has the potentiality to include refined peeling theories as that proposed in Begley et al. (2013). Viscoelastic effects for crazes can also be incorporated as suggested in Allen and Searcy (2001).

From the computational standpoint, based on experimental evidences, the proposed anisotropic cohesive zone model has been included as a constitutive law of a interface element for large displacements, for which a consistent derivation has been developed following the theory published in Reinoso and Paggi (2014) and herein extended to 3D applications. This formulation is deemed to be essential for accurately investigate decohesion and detachment applications undergoing large displacements along with the

coupling of such interface elements with thin-walled element archetypes for the adjoining bulks. In particular, special attention has been devoted to the consistent derivation of the tangent operators stemming from the differentiation of the constitutive equation.

The problem of parameters identification has been discussed in Section 4. Micro-mechanical testing inside a SEM appears to be the only methodology possible to assess the geometrical parameters of the fibrils. Moreover, measurement of the crack-tip opening displacement in single edge-notched specimens under tension allows to experimentally determine the traction-separation law as done by Desai et al. (2011). The use of a tension cut-off cohesive zone model with a peak traction given by the Kendall's solution has been demonstrated to fit reasonably well the experimental trend in case of polymer crazes, although other refined formulations could be used within the same large displacement interface finite element framework.

Finally, two pioneering and exemplary applications of the proposed numerical model have been addressed. The first case analyzed regarded the possibility to exploit the adhesive anisotropy to facilitate debonding of the glass cover in photovoltaic modules for recycling purposes. If a microstructured adhesive with these properties will be technically feasible, then significant energy savings in the dismantling and recycling process of exhausted PV modules are envisaged. The second application focused on the interpretation of the effect of cellulose fibrils anisotropy on the mechanical bonding between paper tissues. This problem has important industrial applications and, so far, there were no computational models able to take into account the action of cellulose fibrils. Future research is ongoing and will regard a close numerical–experimental comparison by performing tensile tests inside a SEM chamber with a tensile stage to monitor the bridging mechanisms of cellulose fibrils during the test. Further applications to bio-interfaces and biological structures are certainly possible, since the proposed formulation has been truly inspired by the physics of natural surfaces.

Acknowledgements

The research leading to these results has received funding from the European Research Council under the European Union's Seventh Framework Programme (FP/2007–2013)/ ERC Grant Agreement n. 306622 (ERC Starting Grant "Multi-field and multi-scale Computational Approach to Design and Durability of PhotoVoltaic Modules" – CA2PVM, PI: Prof. M. Paggi). MP gratefully acknowledges this support. JR would like to acknowledge the financial support by the above ERC Starting Grant, supporting his visiting period at IMT Lucca during March–April 2014, and also the support of the Andalusian Government (Project of Excellence No. TEP-7093) and the Spanish Ministry of Economy and Competitiveness (DPI2012-37187).

Appendix A. Matrix operators for the finite element implementation of the novel interface element for large displacement applications

The matrix operators for the numerical implementation of the present formulation within the framework of FEM are herein provided.

2D interface element

In case of a 2D linear interface element, the shape functions based on the Gauss integration rule are $N_1 = \frac{1}{2}(1-\xi)$ and $N_2 = \frac{1}{2}(1+\xi)$. The previous vectors reduce to:

$$\begin{aligned}
\mathbf{X} &= (X_1, Y_1, X_2, Y_2, X_3, Y_3, X_4, Y_4)^{\mathrm{T}} \\
\mathbf{d} &= (u_1, v_1, u_2, v_2, u_3, v_3, u_4, v_4)^{\mathrm{T}} \\
\mathbf{g}_{\mathrm{loc}} &= (g_{\mathrm{loc,t}}, g_{\mathrm{loc,n}})^{\mathrm{T}} \\
\mathbf{T} &= (\tau, \sigma)^{\mathrm{T}}
\end{aligned} \tag{25}$$

The matrix operators present the following expressions:

$$\mathbf{N} = [N_1\mathbf{I} \quad N_2\mathbf{I}] \tag{26a}$$

$$\mathbf{M} = \frac{1}{2}\begin{bmatrix} \mathbf{I} & \mathbf{0} & \mathbf{0} & \mathbf{I} \\ \mathbf{0} & \mathbf{I} & \mathbf{I} & \mathbf{0} \end{bmatrix} \tag{26b}$$

$$\mathbf{L} = \begin{bmatrix} -\mathbf{I} & \mathbf{0} & \mathbf{0} & \mathbf{I} \\ \mathbf{0} & -\mathbf{I} & \mathbf{I} & \mathbf{0} \end{bmatrix} \tag{26c}$$

where $\mathbf{0}$ is a 2×2 null matrix and $\mathbf{I}$ is a 2×2 identity matrix.

In 2D simulations, the tangential and the normal vectors to the middle surface of the interface element ($\mathbf{t}$ and $\mathbf{n}$) used to define the local frame are:

$$\mathbf{t} = \frac{\partial \overline{\mathbf{x}}^e}{\partial \xi}, \quad \mathbf{n}\cdot\mathbf{t} = 0 \tag{27}$$

Accordingly, the rotation matrix is defined as:

$$\mathbf{R} = \begin{bmatrix} t_x & t_y \\ n_x & n_y \end{bmatrix} \tag{28}$$

where:

$$t_x = n_y = \frac{X_2 + u_2 + X_3 + u_3 - X_1 - u_1 - X_4 - u_4}{2\|\mathbf{t}\|} \tag{29a}$$

$$t_y = -n_x = \frac{Y_2 + v_2 + Y_3 + v_3 - Y_1 - v_1 - Y_4 - v_4}{2\|\mathbf{t}\|} \tag{29b}$$

The operator stemming from the third order tensor renders:

$$\frac{\partial \mathbf{R}}{\partial \mathbf{d}}\mathbf{B}\mathbf{d} = \begin{bmatrix} -a & -b & +a & +b & +a & +b & -a & -b \\ -b & +a & +b & -a & +b & -a & -b & +a \end{bmatrix} \tag{30}$$

where

$$a = \frac{-N_1u_1 - N_2u_2 + N_2u_3 + N_1u_4}{2\|\mathbf{t}\|} \tag{31a}$$

$$b = \frac{-N_1v_1 - N_2v_2 + N_2v_3 + N_1v_4}{2\|\mathbf{t}\|} \tag{31b}$$

3D interface element

In case of a 3D quadrilateral linear interface element, the shape functions corresponding to the Gauss integration rule are:

$$N_1 = \frac{1}{4}(1-\xi)(1-\eta) \tag{32a}$$

$$N_2 = \frac{1}{4}(1+\xi)(1-\eta) \tag{32b}$$

$$N_3 = \frac{1}{4}(1+\xi)(1+\eta) \tag{32c}$$

$$N_4 = \frac{1}{4}(1-\xi)(1+\eta) \tag{32d}$$

The vectors previously defined reduce to:

$$\mathbf{X} = (X_1, Y_1, \ldots, X_8, Y_8)^{\mathrm{T}} \tag{33a}$$

$$\mathbf{d} = (u_1, v_1, \ldots, u_8, v_8)^{\mathrm{T}} \tag{33b}$$

$$\mathbf{g}_{\mathrm{loc}} = (g_{\mathrm{loc},t_1}, g_{\mathrm{loc},t_2}, g_{\mathrm{loc},n})^{\mathrm{T}} \tag{33c}$$

$$\mathbf{T} = (\tau_1, \tau_2, \sigma)^{\mathrm{T}} \tag{33d}$$

The matrix operators for the 3D formulation present the following expressions:

$$\mathbf{N} = [N_1\mathbf{I} \quad N_2\mathbf{I} \quad N_3\mathbf{I} \quad N_4\mathbf{I}] \tag{34a}$$

$$\mathbf{M} = \frac{1}{2}\begin{bmatrix} \mathbf{I} & \mathbf{0} & \mathbf{0} & \mathbf{0} & \mathbf{I} & \mathbf{0} & \mathbf{0} & \mathbf{0} \\ \mathbf{0} & \mathbf{I} & \mathbf{0} & \mathbf{0} & \mathbf{0} & \mathbf{I} & \mathbf{0} & \mathbf{0} \\ \mathbf{0} & \mathbf{0} & \mathbf{I} & \mathbf{0} & \mathbf{0} & \mathbf{0} & \mathbf{I} & \mathbf{0} \\ \mathbf{0} & \mathbf{0} & \mathbf{0} & \mathbf{I} & \mathbf{0} & \mathbf{0} & \mathbf{0} & \mathbf{I} \end{bmatrix} \tag{34b}$$

$$\mathbf{L} = \begin{bmatrix} -\mathbf{I} & \mathbf{0} & \mathbf{0} & \mathbf{0} & \mathbf{I} & \mathbf{0} & \mathbf{0} & \mathbf{0} \\ \mathbf{0} & -\mathbf{I} & \mathbf{0} & \mathbf{0} & \mathbf{0} & \mathbf{I} & \mathbf{0} & \mathbf{0} \\ \mathbf{0} & \mathbf{0} & -\mathbf{I} & \mathbf{0} & \mathbf{0} & \mathbf{0} & \mathbf{I} & \mathbf{0} \\ \mathbf{0} & \mathbf{0} & \mathbf{0} & -\mathbf{I} & \mathbf{0} & \mathbf{0} & \mathbf{0} & \mathbf{I} \end{bmatrix} \tag{34c}$$

where $\mathbf{0}$ is a 3×3 null matrix and $\mathbf{I}$ is a 3×3 identity matrix.

In 3D cases, the tangential and the normal vectors to the middle surface of the interface element ($\mathbf{t}_1, \mathbf{t}_2$ and $\mathbf{n}$) used to define the local frame are determined via differentiation of the average coordinates with respect to the natural coordinates ξ and η:

$$\mathbf{t}_1 = \frac{\partial \overline{\mathbf{x}}^e}{\partial \xi}, \quad \mathbf{t}_2 = \frac{\overline{\mathbf{x}}^e}{\partial \eta}, \quad \mathbf{n} = \mathbf{t}_1 \times \mathbf{t}_2 \tag{35}$$

Therefore the rotation matrix reads:

$$\mathbf{R} = \begin{bmatrix} t_{1,x} & t_{1,y} & t_{1,z} \\ t_{2,x} & t_{2,y} & t_{2,z} \\ n_x & n_y & n_z \end{bmatrix} \tag{36}$$

where the coefficients are computed according to definitions in Eq. (27).

The operator stemming from the third order tensor has to be derived with care since it brings the contribution of several terms. Therefore, a closed form expression of the operator after the various derivatives and matrix multiplications is difficult to be expressed in a condense form. It is more convenient to define vectors containing the partial derivatives of the components of the rotation matrix with respect to the nodal displacements and use them for the subsequent matrix multiplications to be performed numerically.

References

Allen, D.H., Searcy, C.R., 2001. A micromechanical model for a viscoelastic cohesive zone. Int. J. Fract. 107, 159–176.

Balzani, C., Wagner, W., 2008. An interface element for the simulation of delamination in unidirectional fiber-reinforced composite laminates. Eng. Fract. Mech. 75, 2597–2615.

Begley, M.R., Collino, R.R., Israelachvili, J.N., McMeeking, R.M., 2013. Peeling of a tape with large deformations and frictional sliding. J. Mech. Phys. Solids 61, 1265–1279.

Bertoldi, K., Bigoni, D., Drugan, W.J., 2007a. Structural interfaces in linear elasticity. Part I: Nonlocality and gradient approximations. J. Mech. Phys. Solids 55, 1–34.

Bertoldi, K., Bigoni, D., Drugan, W.J., 2007b. Structural interfaces in linear elasticity. Part II: Effective properties and neutrality. J. Mech. Phys. Solids 55, 35–63.

Bertoldi, K., Bigoni, D., Drugan, W.J., 2007c. A discrete-fibers model for bridged cracks and reinforced elliptical voids. J. Mech. Phys. Solids 55, 1016–1035.

Bigoni, D., Movchan, A.B., 2002. Statics and dynamics of structural interfaces in elasticity. Int. J. Solids Struct. 39, 4843–4865.

Chen, A., Gao, H., 2007. Bio-inspired mechanics of reversible adhesion: orientation-dependent adhesion strength for non-slipping adhesive contact with transversely isotropic elastic materials. J. Mech. Phys. Solids 55, 1001–1015.

Chen, B., Wu, P.D., Gao, H., 2008. Hierarchical modelling of attachment and detachment mechanisms of gecko toe adhesion. Proc. Roy. Soc. London A 464, 1639–1652.

Creton, C., Lakrout, H., 2000. Micromechanics of flat-probe adhesion tests of soft viscoelastic polymer films. J. Polym. Sci. Part B: Polym. Phys. 38, 965–979.

Desai, C.K., Kumar, A.S., Basu, S., Parameswaran, V., 2011. Measurement of cohesive parameters of crazes in polystyrene films. Exp. Appl. Mech., Conf. Proc. Soc. Exp. Mech. Ser. 6, 519–526.

Estevez, R., Tijssens, M.G.A., van der Giessen, E., 2000. Modeling of the competition between shear yielding and crazing in glassy polymers. J. Mech. Phys. Solids 48, 2585–2617.

Gao, H., Ji, B., Buehler, M.J., Yao, H., 2004. Flaw tolerant bulk and surface nanostructures of biological systems. Mech. Chem. Biosyst. 1, 37–52.

Gao, H., Wang, X., Yao, H., Gorb, S., Arzt, E., 2005. Mechanics of hierarchical adhesion structure of gecko. Mech. Mater. 37, 275–285.

Gillies, A.G., Fearing, R.S., 2014. Simulation of synthetic gecko arrays shearing on rough surfaces. J. Roy. Soc. Interface 11, 20140021.

Hoefnagels, J.P.M., Neggers, J., Timmermans, P.H.M., van der Sluis, O., Geers, M.G.D., 2010. Copper–rubber interface delamination in stretchable electronics. Scr. Mater. 63, 875–878.

Huber, G., Gorb, S., Spolenak, R., Arzt, E., 2005. Resolving the nanoscale adhesion of individual gecko spatulae by atomic force microscopy. Biol. Lett. 1, 2–4.

Kendall, K., 1975. Thin-film peeling – the elastic term. J. Phys. D: Appl. Phys. 8, 1449–1452.

Kramer, H.H., Berger, L.L., 1990. Craze growth and fracture. Adv. Polym. Sci. 91 (92), 1–68.

Lepore, E., Pugno, F., Pugno, N., 2012. Optimal angles for maximal adhesion in living tokay geckos. J. Adhesion 88, 820–830.

Matous, K., Kulkarni, M.G., Geubelle, P.H., 2008. Multiscale cohesive failure modeling of heterogeneous adhesives. J. Mech. Phys. Solids 56, 1511–1533.

Ortiz, M., Pandolfi, A., 1999. Finite deformation irreversible cohesive elements for three-dimensional crack-propagation analysis. Int. J. Numer. Methods Eng. 44, 1267–1282.

Paggi, M., Berardone, I., Infuso, A., Corrado, M., 2014. Fatigue degradation and electric recovery in Silicon solar cells embedded in photovoltaic modules. Sci. Rep. 4, 1–7 (paper no. 04506).

Paggi, M., Corrado, M., Rodriguez, M.A., 2013. A multi-physics and multi-scale numerical approach to microcracking and power-loss in photovoltaic modules. Compos. Struct. 95, 630–638.

Paggi, M., Wriggers, P., 2011a. A nonlocal cohesive zone model for finite thickness interfaces – Part I: mathematical formulation and validation with molecular dynamics. Comput. Mater. Sci. 50, 1625–1633.

Paggi, M., Wriggers, P., 2011b. A nonlocal cohesive zone model for finite thickness interfaces – Part II: FE implementation and application to polycrystalline materials. Comput. Mater. Sci. 50, 1634–1643.

Paggi, M., Wriggers, P., 2012. Stiffness and strength of hierarchical polycrystalline materials with imperfect interfaces. J. Mech. Phys. Solids. 60, 557–572.

Pugno, N., Lepore, E., 2008. Observation of optimal gecko's adhesion on nanorough surfaces. Biosystems 94, 218–222.

Pugno, N., Lepore, E., Toscano, S., Pugno, F., 2011. Normal adhesive force-displacement curves of living geckos. J. Adhesion 87, 1059–1072.

Qiu, Y., Crisfield, M.A., Alfano, G., 2001. An interface element formulation for the simulation of delamination with buckling. Eng. Frac. Mech. 68, 1755–1776.

Reinoso, J., Paggi, M., 2014. A consistent interface element formulation for geometrical and material nonlinearities. Comput. Mech. 54, 1569–1581.

Scherge, M., Gorb, S., 2001. Biological Micro- and Nanotribology. Springer, New York.

van den Bosch, M.J., Schreurs, P.J.G., Geers, M.G.D., 2007. A cohesive zone model with a large displacement formulation accounting for interfacial fibrilation. Eur. J. Mech. A/Solids 26, 1–19.

van den Bosch, M.J., Schreurs, P.J.G., Geers, M.G.D., 2008a. On the development of a 3D cohesive zone element in the presence of large deformations. Comput. Mech. 42, 171–180.

van den Bosch, M.J., Schreurs, P.J.G., Geers, M.G.D., 2008b. Identification and characterization of delamination in polymer coated metal sheet. J. Mech. Phys. Solids 56, 3259–3276.

Vossen, B.G., Schreurs, P.J.G., van der Sluis, O., Geers, M.G.D., 2014. Multi-scale modeling of delamination through fibrillation. J. Mech. Phys. Solids 66, 117–132.

Yao, H., Della Rocca, G., Guduru, P.R., Gao, H., 2008. Adhesion and sliding response of a biologically inspired fibrillar surface: experimental observations. J. Roy. Soc. Interface 5, 723–733.

Yao, H., Gao, H., 2006. Mechanics of robust and releasable adhesion in biology: bottom-up designed hierarchical structures of gecko. J. Mech. Phys. Solids 54, 1120–1146.

Yao, H., Gao, H., 2007. Mechanical principles of robust and releasable adhesion of gecko. J. Adhesion Sci. Technol. 21, 1185–1212.

Yao, H., Gao, H., 2008. Multi-scale cohesive laws in hierarchical materials. Int. J. Solids Struct. 45, 3627–3643.

Zienkiewicz, O.C., Taylor, R.L., 2004. The Finite Element Method, Solid Mechanics, fifth ed., vol. 2. Butterworth Heinemann, Oxford, UK.

Zhou, Y., Robinson, A., Steiner, U., Federle, W., 2014. Insect adhesion on rough surfaces: analysis of adhesive contact of smooth and hairy pads on transparent microstructured substrates. J. Roy. Soc. Interface 11, 20140499.